Nanoscale

PAPER

View Article Online
View Journal

Cite this: DOI: 10.1039/d0nr02133d

Identification of a moderate affinity CD22 binding peptide and *in vitro* optimization of peptide-targeted nanoparticles for selective uptake by CD22+ B-cell malignancies†

Baksun Kim,‡[a] Jaeho Shin,‡[a] Tanyel Kiziltepe[a,b,c] and Basar Bilgicer *[a,b,c]

B cell malignancies, such as B cell leukemia and lymphoma, have CD22 overexpression with ~7% of patients. A short CD22 binding peptide (PV3) with a moderate affinity (K_d ~ 9 μM) was identified by screening multiple peptide candidates determined through analysis of CD22-epratuzumab complex crystal structure. PV3 binding specificity was confirmed *via* competitive binding inhibition, then was used as the targeting moiety on CD22-targeted liposomal nanoparticle (TNP^{PV3}) formulations. To maximize the potential therapeutic outcome of TNP^{PV3} formulation, nanoparticle design parameters, such as peptide hydrophilicity, ethylene glycol linker length, valency, and particle size were optimized for maximum selective cellular uptake by CD22+ malignant cancer cells. The effects of altering design parameters one at a time on TNP uptake were evaluated using flow cytometry, and the optimal parameters for TNP^{PV3} were determined to be 8% peptide density, EG18 linker, and 3 lysines of 100 nm nanoparticles. This optimally designed TNP^{PV3} achieved ~4 and 40-fold enhancement of cellular uptake by CD22+ Raji cells over CD22– Jurkat and MOLT-4 cells, respectively, demonstrating selectivity for malignant cells with CD22 overexpression. Overall, this study establishes PV3 to be CD22 binding peptide with proven effectiveness as a targeting element. In future, the optimal TNP^{PV3} formulation will potentially achieve maximal *in vivo* therapeutic outcomes by efficiently targeting CD22+ blood cancer cells *in vivo*.

Received 16th March 2020,
Accepted 19th May 2020

DOI: 10.1039/d0nr02133d

rsc.li/nanoscale

Introduction

Here, we report a peptide-targeted nanoparticle design that has an enhanced selectivity for cluster of differentiation 22 (CD22)-expressing malignant B-cells using a novel CD22 binding peptide (PV3), which was identified *via* analysis of crystal structure of CD22 antigen–anti-CD22 antibody complex. B-cell malignancies are a collection of blood cancers exhibiting abnormal behaviors of B lymphocytes in their cell growth, proliferation, and function.[1] Over the past decades, several different approaches to treat B-cell malignancies have been developed, such as B-cell associated leukemias and lymphomas. Monoclonal antibody (mAb)–targeted therapies and chimeric antigen receptor T cell immunotherapies are such treatments that have shown to improve patient outcome relative to conventional chemotherapies.[2–7] Despite ongoing efforts, several critical issues remain unresolved. For instance, lack of selectivity for malignant B-cells over healthy B-cells is one of the significant challenges that needs to be addressed since it results in an increased likelihood of unforeseen systemic toxicities and poor clinical outcomes.[8–12]

As an alternative to available treatments, receptor-targeted nanoparticle (TNP) drug delivery systems have also been investigated to improve efficacy for B-cell malignancies.[13–22] This strategy employs multivalency–targeting moieties on the nanoparticle surfaces form multiple interactions with target receptors–to promote the nanoparticles to be internalized into the cancerous cells to selectively deliver the drug payload.[23] To date, although TNP-based drug delivery systems have shown a promise in preclinical studies, none of the research outcomes have past advanced clinical trials.[24] This is mainly due to the reduced selectivity for malignant B-cells from using targeting moieties that have high affinities, such as mAbs, for TNP platform.[13–22] Despite high affinity targeting elements having a high specificity for a target receptor, they bind to not only the target receptors that are overexpressed on malignant

[a]*Department of Chemical and Biomolecular Engineering, University of Notre Dame, Notre Dame, IN 46556, USA. E-mail: bbilgicer@nd.edu*
[b]*Harper Cancer Research Institute, University of Notre Dame, Notre Dame, IN 46556, USA*
[c]*Advanced Diagnostics and Therapeutics, University of Notre Dame, Notre Dame, IN 46556, USA*

†Electronic supplementary information (ESI) available. See DOI: 10.1039/d0nr02133d

‡These two authors contributed equally to this work and are co-first authors

B-cells but also the same receptors that are expressed on healthy B-cells.[8–12] This results in TNP adhering to healthy B-cells non-selectively and causes an increased probability of off-target toxicities, thus hindering successful translation into the clinic. In addition, most of TNP production methods likely result in inconsistent and unreliable experimental outcomes, due to batch-to-batch variability in conjugation yield of targeting elements to the nanoparticle platform.[24] Consequently, enhancement in selectivity for cancerous cells with reproducible TNP productions is a key point to achieve not only an enhanced efficacy but also a consistent and improved overall patient outcome.

To address the selectivity issue, our strategy is to use a specific receptor binding peptide as a targeting moiety on TNPs. Peptides are well-suited candidates as the targeting ligands due to low molecular weight, ease of synthesis, specificity, and low immunogenicity.[25] Most importantly, we can take advantage of their weak-to-moderate binding affinities for our multivalent targeting approach. Moderate affinity provides a short dissociation half-live which results in TNP to have a short residence time for staying to receptors presented on surfaces at lower densities, preventing TNP from getting endocytosed by healthy cells.[23,26] In contrast, once the same TNP encounters a malignant B-cell with relatively higher expression level of the target receptor, several peptides simultaneously form multiple binding interactions. These multivalent interactions provide an enhanced avidity to enable the nanoparticle to stay on the cellular surface for an extended time, thereby internalizing selectively into the cancerous cells for delivery of the drug payload.[23,26]

CD22 is a transmembrane glycoprotein that belongs to a Siglec-family lectin and expressed on the surface of pre and mature B-cells, except plasma cells.[27–29] CD22 consists of 7 immunoglobulin-like extracellular domains, containing a domain responsible for alpha 2,6 sialic-acid ligand binding.[27–29] CD22 has recently emerged as an attractive therapeutic target since it is expressed on most of malignant B-cells including non-Hodgkin's lymphoma (NHL), Burkitt's lymphoma, B-cell acute lymphoblastic leukemia (B-ALL), *etc*.[27–29] More interestingly, it has been reported that despite the expression levels of CD22 varying upon patients, its relatively higher expression on malignant B-cells was observed in ~7–11% of total study populations in comparison with normal B-cells.[30,31] This further provides a support for CD22 as an excellent target receptor for multivalent TNP systems to B-cell malignancies.

Currently, many research groups have introduced CD22 targeting ligands with high affinity, such as anti-CD22 antibodies, however, there are no reported CD22 binding peptides with moderate affinities that could effectively target CD22 receptor. Hence, the objectives of our study were to (i) identify CD22-specific peptide with moderate affinity; and (ii) *in vitro* evaluate therapeutic potentials of CD22 TNPs for B-cell malignancies using the identified peptide. Here, we report a CD22 specific peptide (PV3) with a moderate affinity (~9 μM) that was identified *via* systematic analysis of 3D crystal structure of anti-CD22 antibody-CD22 receptor complex.[32] To achieve consistent experimental outcomes, we employed our synthetic strategy that produces highly pure, reproducible and precisely controlled TNPs. To find the optimal formulations of PV3 presenting CD22 TNP (TNP^{PV3}) that enhance malignant B-cell uptake, we investigated the effects of crucial nanoparticle design parameters on cellular binding and uptake *in vitro*, such as nanoparticle size, peptide ethylene glycol (EG) linker length, peptide hydrophilicity, and peptide density. The results establish PV3 to be an CD22 specific peptide, and optimally designed TNP^{PV3} both effectively and selectively binds to CD22-positive (CD22+) malignant B cells.

Materials and methods

Materials

NovaPEG Rink Amide low loading resin, 2-(1*H*-benzotriazol-1-yl)-1,1,3,3 tetramethyluroniumhexafluorophosphate (HBTU), and all Fmoc-protected amino acids were purchased from EMD Millipore. *N*,*N*-Dimethylformamide (DMF), dichloromethane (DCM), *N*,*N*-diisopropylethylamine (DIEA), trifluoroacetic acid (TFA), 2-propanol (IPA), acetonitrile (ACN), methanol, piperidine, Kaiser test reagents, triisopropylsilane (TIS), PBS, ethanol, and cholesterol were purchased from Sigma-Aldrich. We purchased 1,2-distearoyl-*sn-glycero*-3-phosphocholine (sodium salt) (DSPC) and 1,2-distearoyl-*sn-glycero*-3-phosphoethanolamine-*N*-[methoxy (polyethylene glycol)-2000] (ammonium salt) (mPEG2000-DSPE) from Avanti Polar Lipids. 3*H*-Indolium, 2-(5-(1,3-dihydro-3,3-dimethyl-1-octadecyl-2*H*-indol-2-ylidene)-1,3-pentadienyl)-3,3-dimethyl-1-octadecyl-perchlorate (DiD fluorescent dye) was obtained from Invitrogen. Fluorescein 5-isothyocyanate (FITC) was purchased from Toronto Research Chemicals. All Fmoc-*N*-amido-$dPEG_N$-acids were purchased from Quanta Biodesign.

Synthesis of CD22 binding Pep-FITC and lipid conjugates

Peptides were synthesized using Fmoc chemistry based-solid phase peptide synthesis methods as previously described.[33] Molecules were cleaved from the solid support using 95/2.5/2.5 of TFA/H_2O/TIS mixture and then purified using RP-HPLC on an Agilent 1200 series system with a semipreparative Zorbax C18 column and C3 column with acetonitrile (4% min^{-1}) and 2-propanol (4% min^{-1}) gradients, respectively in the mobile phase. Bruker microTof-Q II was used to characterize the products. Their purities were evaluated by RP-HPLC analytical injections with Zorbax C3 column.

Preparation of liposomal nanoparticles

Liposomal nanoparticles were prepared using a thin film method as reported previously.[33] Briefly, mixture of DSPC, mPEG2000-DSPE, CD22 peptide–lipid conjugates, DiD, and cholesterol was prepared in a glass vial and dried by nitrogen gas into a thin film. Then, it was hydrated with PBS (pH 7.4) at 68 °C and followed by extrusion through polycarbonate filter membranes with Avanti Polar Lipid extruder set. Liposomes were formulated as the following molar ratio: $(94.9-x)/5/x/0.1$ of DSPC/mPEG2000-DSPE/CD22 peptide–lipid conjugates/DiD dye where x was varied from 0 to 10 as the peptide densities. Non-targeted liposomes were always prepared as controls with

the molar ratio of 95/5 of DSPC/mPEG2000-DSPE. All nanoparticles were incorporated with an additional 5% cholesterol of total phospholipid concentration.

Characterization of nanoparticles

Nanoparticle size was measured by dynamic light scattering (DLS), NanoBrook Omni Particle Size Analyzer (Brookhaven Instruments Corp.) as described previously.[33] For evaluating peptide loading efficiency in TNPs, liposomal nanoparticles were prepared and purified as described previously.[34] The CD22 peptide–lipid conjugates loaded on nanoparticles were measured by RP-HPLC at 220 nm and 280 nm. Then, the absorbance intensity was compared to that of theoretical maximum concentration of CD22 peptide–lipid conjugates to evaluate loading efficiency.

Cell culture

Raji, Jurkat, and MOLT-4 cells were purchased from American Type Culture Collection (ATCC) and cultured in RPMI 1640 media (Gibco). All lines were supplemented with 10% fetal bovine serum (Gemini), 2 mM L-glutamine (Gibco), 100 U ml^{-1} penicillin, and 100 μg ml^{-1} streptomycin (Gibco).

In vitro peptide cellular binding assay

Fluorescein labeled peptides were incubated with cells (1×10^5 cells per well) in blocking buffer (1.5% BSA in PBS pH 7.4) at increasing concentration for 1 h on ice. Then, the samples were washed with PBS (pH 7.4) and analyzed on Guava easyCyte 8HT flow cytometer (Millipore).

In vitro liposomal nanoparticle cellular uptake assay

In vitro cellular uptake assay was performed as described previously.[33] 1×10^5 cells per well were plated in a 24 well dish in 37 °C incubator overnight. Nanoparticles were incubated with cells for 3 h at 37 °C. DiD (0.1% total phospholipid) was incorporated to quantify nanoparticle cellular uptake. After incubation, cells were trypsinized to remove nanoparticles bound on cell surface, washed twice with PBS (pH 7.4), and analyzed *via* flow cytometer. For competitive inhibition assay, 50 μM of free peptides with the respective peptide sequence was added 30 min prior to nanoparticle addition, followed by the same cellular uptake assay as described above.

Results and discussion

Identifying CD22 binding peptide sequences

To identify potential CD22 binding peptides, we analyzed the crystal structure (PDB ID: 5VL3) of CD22-epratuzumab complex (a humanized monoclonal CD22 targeting antibody). Specifically, we studied Fab of epratuzumab heavy-chain complementarity determining regions (HCDRs) due to generally more significant interactions with antigens over light-chain

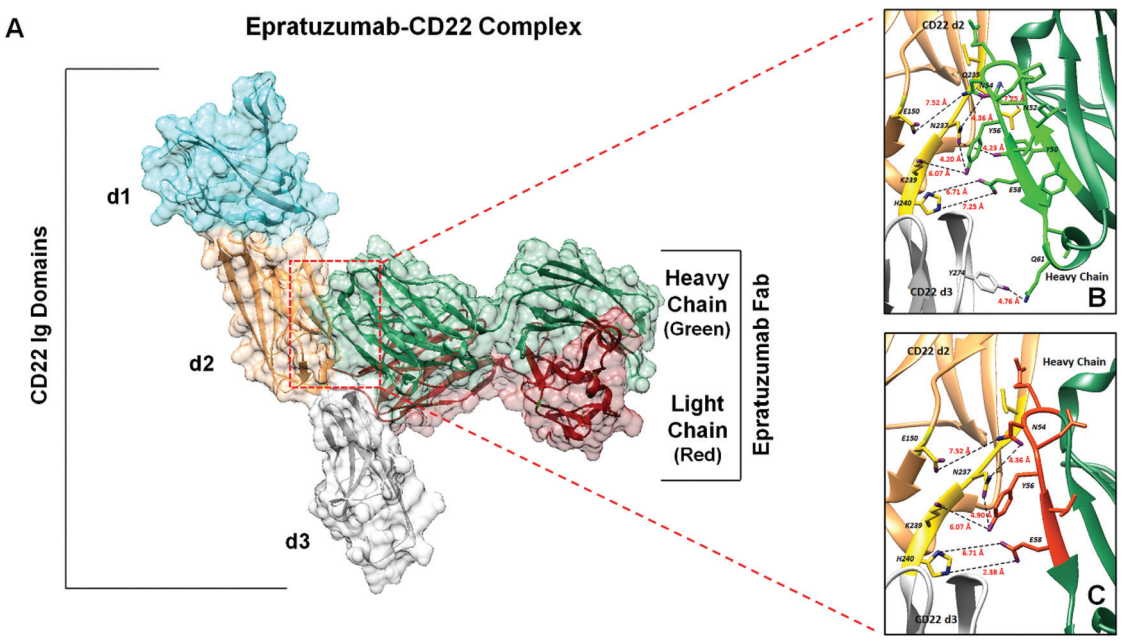

Fig. 1 Analysis of crystal structure of epratuzumab-CD22 complex. To identify potential CD22 binding peptide sequences, we analyzed the molecular interactions between epratuzumab (anti-CD22 antibody) and CD22 antigen on the crystal structure available in protein data bank (PDB ID: 5VL3). (A) Crystal structure of epratuzumab-CD22 complex. Three Ig-like domains of CD22 antigen (d1 (cyan), d2 (light brown), and d3 (gray)) interact with amino acid residues on both heavy (green) and light (red) chains of epratuzumab Fab region. (B) and (C) show the three potential CD22 binding sequences (PV1, PV2, and PV3). Through analysis of the structure, several potential molecular interactions were recognized in between d2 and heavy chain complementarity determining region 2 (HCDR2). Specific amino acid residues (yellow) on d2 interact with the counterparts on HCDR2. Bright green shown in (B) indicates the peptide sequence for both PV1 (a linear version) and PV2 (a cyclic version) while orange in (C) shows the peptide sequence of PV3.

complementarity determining regions (LCDRs).[35–37] Among the epratuzumab HCDRs, we isolated three potential CD22 binding peptides, denoted PV1, PV2, and PV3, from HCDR2 which showed a greater number of molecular interactions with CD22 in proximity over HCDR1 and HCDR3 (Fig. 1 and 2A, B).

PV1 peptides (GYINPRNDYTEYNQ, 49–61) showed extensive interactions over CD22 domain 2 (d2) and domain 3 (d3) by possessing potential hydrogen bonding (H-bond) interactions as the followings: (Y50–N237, 4.23 Å), (N52–Q235, 7.25 Å), (N54–E150/N237, 7.52 Å/4.36 Å), (Y56–N237/K239, 4.20 Å/6.07 Å), (E58–H240, 6.71 Å/7.25 Å), and (Q61–Y274, 4.76 Å), which makes PV1 as a potential candidate of CD22 binding peptides.

In addition to linear conformation PV1 peptides, the crystal structure demonstrates PV1 as a loop while interacting with CD22. Therefore, we synthesized cyclized version of PV1 peptides, named PV2, to mimic HCDR2 loop which may enhance binding efficiency on CD22. Furthermore, cyclization of peptides has shown improved binding affinities by reducing conformational entropic penalties which makes PV2 as another promising CD22 binding peptides.[38,39] For this purpose, we modified PV1 by conjugating cysteine next to G49 and replacing Y59 with another cysteine to form disulfide bond. Furthermore, I51 and T57 were replaced with arginine to improve stability of beta strands of PV2 as well as increasing solubility of peptides which potentially enhance its binding efficiency.

Although PV1 and PV2 peptides possess multiple significant interactions with CD22, they also have several non-interacting amino acid residues: N60, Y59, P52a, I51, G49, which could potentially increase non-specificity of the peptides. Therefore, we isolated a short linear version (RNDYTE, 53–58) from PV1, named PV3, which possesses most of H-bond interactions with CD22 d2 while minimizing non-interacting residues. With its short sequence, we expected PV3 to have relatively weaker affinity compared to PV1 and PV2, but we hypothesized that PV3 might be more specific to CD22 which may offset its weaker affinity to have improved binding efficiency.

Evaluating CD22 targeting peptide binding with CD22+ cells

To examine binding of the peptide candidates to CD22, we performed peptide cellular binding assay using flow cytometry. Fluorescently labeled peptides were incubated with Raji (CD22+) on ice for 1 hour, and peptide cellular binding was analyzed by flow cytometry. Control experiments with fluorescently labeled scrambled peptides showed only minimal background binding which was subtracted from the data point. Our results showed no detectable binding of PV1 and PV2 on Raji, while PV3 bound to Raji cell line with an apparent K_d of ~9 μM (Fig. 2C). Among the candidates, due to its specificity

A

Peptides	# Residues	Sequences
PV1	49-61	GYINP*RNDYTEYNQ
PV2	49-61**	CGYRNP*RNDYRECNQ
PV3	53-58	RNDYTE

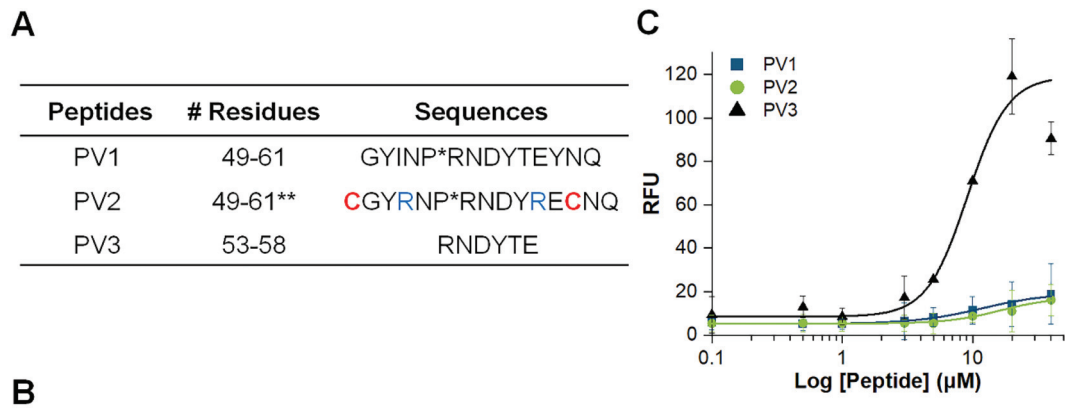

Fig. 2 Evaluation of CD22 targeting peptide binding with CD22+ cells. (A) Amino acid sequences of PV1, PV2, and PV3. The amino acid sequences of PV1, PV2, and PV3 were identified through analysis of HCDR2. The amino acid sequence of PV1 was modified to generate a cyclic version, PV2. Two cysteine residues (C, red) were added in the original sequence (PV1) for cyclization, while two arginines (R, blue) were replaced with isoleucine (I) and threonine (T) to enhance the peptide's structural stability and binding efficacy. PV3 derived from PV1 has a shorter sequence due to more converged multiple significant interactions relative to the PV1. (B) Chemical structure of CD22 targeting peptides. (C) Binding affinity study of peptides with CD22+ cells. Binding assay was performed on ice by observing fluorescently labeled peptide's interaction (relative fluorescence unit, RFU) with Raji cell line (CD22+) using flow cytometry. All experiments were performed in triplicates, and data represents means (±s.d.). Asterisk (*) indicates that proline residue is positioned at 52a in the crystal structure. Two asterisks (**) indicate that PV2 is a cyclic version peptide derived from PV1.

and moderate affinity to CD22 positive cells, PV3 peptides have potential to be utilized as CD22 targeting moieties on nanoparticles, which will be further evaluated in this study using nanoparticle cellular uptake assays.

Design and synthesis of CD22 TNPs

As described in Fig. 3, liposomal nanoparticles can selectively target cancerous B cells over healthy cells by optimizing design parameters. When nanoparticles encounter healthy cells while they circulate in the blood stream, the optimized peptide valency on the nanoparticles would promote monovalent interactions with CD22 on healthy cells. Then, due to short dissociation half-life of peptides and low CD22 expression level, the monovalent interaction may not provide the nanoparticles with enough residence time to stay in bound. As a result, the nanoparticles are likely to dissociate from healthy cells. On the other hand, when the nanoparticles approach cancerous B cells expressing higher level of CD22, the optimized valency enhance multiple interactions with CD22 simultaneously which increase avidity of the nanoparticle to reside on the cancer cell surface for a longer time. In this way, the nanoparticles will eventually internalize into cancer cells and deliver drug payload. Therefore, optimization of nanoparticles is a critical step to achieve selective targeting, thereby maximizing drug efficacy on cancerous B cells while minimizing systemic toxicity.

To synthesize optimized nanoparticles, peptide properties and linkers are important liposome design parameters.[38,39] Furthermore, it is critical to be able to produce precise liposomal formulations with batch-to-batch consistency to achieve reproducible experimental results. For this purpose, we first synthesized peptide–lipid conjugates prior to preparing liposomes (Fig. 4A).[33,38,39] In our design, peptides are first conjugated to oligolysines (K_N) *via* EG2 spacer. EG2 spacer is to minimize interaction between peptides and oligolysines. Lysine residues enhance hydrophilicity of targeting peptides to be efficiently exposed above polyethylene glycol (PEG) cloud (stealth coating on a nanoparticle surface to prevent reticuloendothelial system (RES) clearance) for improved availability and binding efficiency. Then, peptides-EG2-K_N moieties are conjugated to palmitic acid *via* an EG linker. EG Linkers enable targeting peptides to be presented above PEG cloud. Two hydrophobic fatty chains of palmitic acid enable insertion of peptide–lipid conjugates into lipid bilayer of liposomes. Synthetic procedures were performed using solid phase peptide synthesis protocols with Fmoc chemistry. Products were purified by RP-HPLC and characterized by mass spectrometry. Their purities were determined to be >95% by analytical HPLC column (Table ST1†).

CD22 TNPs were prepared using a thin lipid film method (Fig. 4B). First, peptide–lipid conjugates were mixed with other

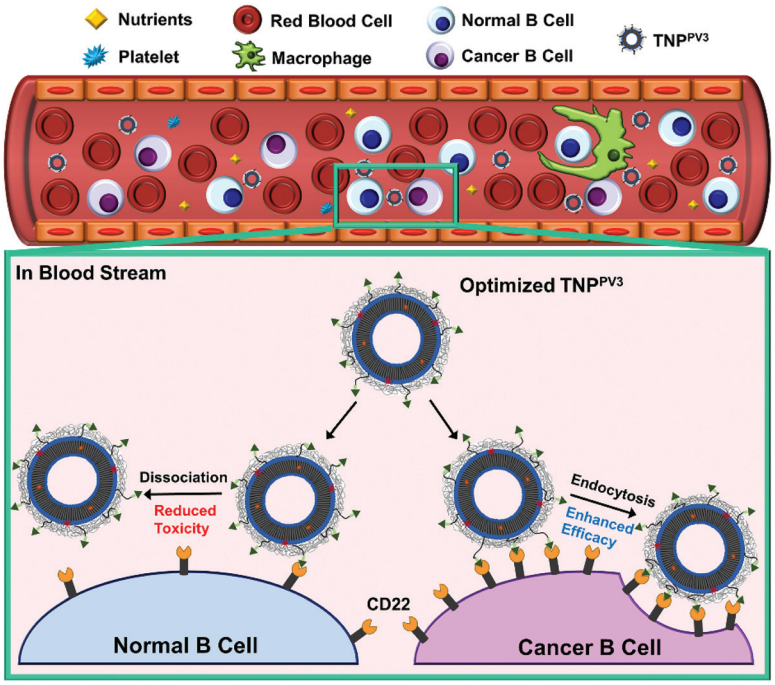

Fig. 3 A cartoon representing strategy of TNP^{PV3} selective targeting on CD22+ malignant B-cells. In B-cell malignancies, cancerous B cells typically have higher expression levels of CD22 compared to healthy B cells. Due to peptide's short dissociation half-life with the CD22 receptor, when TNP^{PV3} binds to a CD22 receptor on a healthy B cell surface, due to the low expression levels, the interaction will be monovalent in its nature and won't give TNP^{PV3} enough residence time for subsequent endocytosis. On the other hand, when the same TNP^{PV3} comes across a cancerous cell expressing higher levels of CD22, multiple PV3 peptides will simultaneously interact with multiple CD22 receptors, providing the particle with enhanced avidity and promote it to reside on the cancer cell surface for a longer time, thereby facilitating endocytosis for the delivery of the drug-payload inside the cancer cell. Therefore, this approach is designed to provide enhanced selectivity for cancerous B cells over healthy B cells, which should achieve increased efficacy with minimized systemic toxicity.

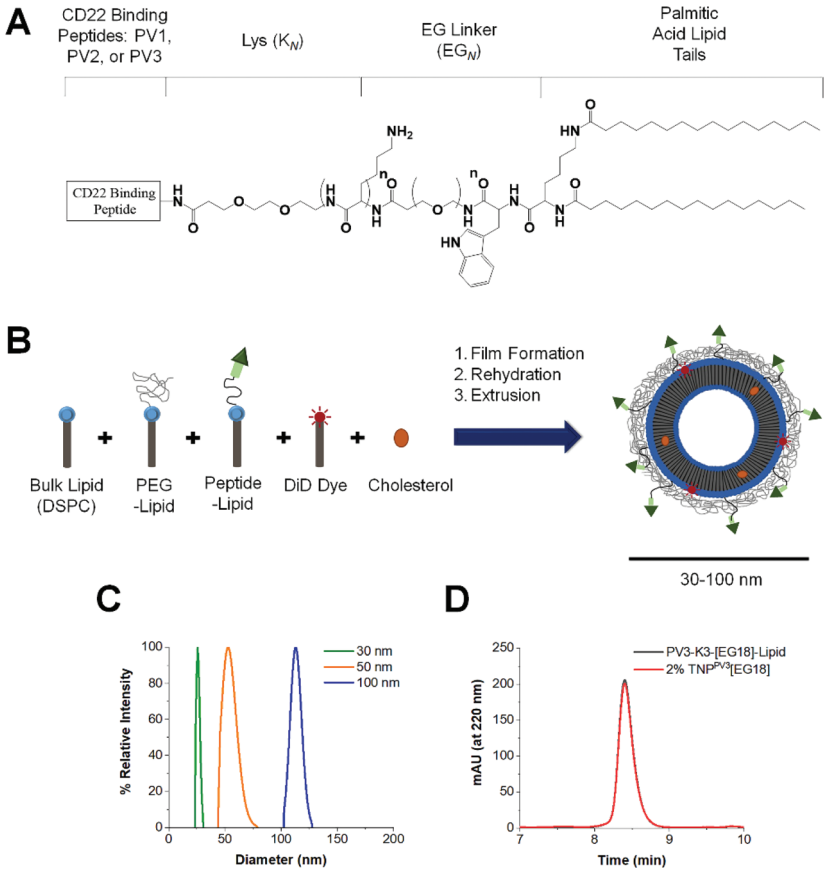

Fig. 4 Design and synthesis of CD22 TNPs. (A) Design of the peptide–lipid conjugate. To improve the accessibility of the targeting peptide to promote binding, its partitioning into the aqueous phase was increased by introducing charged groups using lysine residues. Targeting peptide was separated from oligolysine (K_N) with an EG2 spacer to prevent potential interference during binding. Another EG linker (EG_N, N is the repeating unit of ethylene glycol where $0 \leq N \leq 45$) was used to conjugate the peptide-EG2-K_N moiety to two palmitic acid tails that anchor the peptide-construct on the liposome. The EG linkers provide conformational flexibility to accommodate multivalent peptide binding. (B) Formulation of CD22 TNPs. CD22 TNPs were generated in three main steps. First, a dried lipid film was formed that incorporates a mixture of pure components (peptide–lipid conjugate, fluorophore-lipid conjugate, cholesterol, and DSPC) at specific stoichiometries. The lipid film was then rehydrated in PBS and extruded *via* a polycarbonate membrane to produce CD22 TNPs of specified sizes. (C) Particle size analysis of CD22 TNPs. DLS (dynamic light scattering) analysis of CD22 TNPs indicated the specified sizes were achieved with narrow polydispersity. (D) Peptide loading efficiency. RP-HPLC was used to quantify the amount of targeting peptide loaded in each formulation and confirmed that TNPs contained the intended percent of targeting peptide. Data shows a representative experiment.

pure components including, DSPC, mPEG2000-DSPE, and cholesterol at a specific stoichiometry and dried completely into a thin film. The liposomal nanoparticles were prepared in the following molar ratios: $(94.9 - x)\%/5\%/x\%/0.1\%$ of DSPC/mPEG2000-DSPE/peptide–lipid/DiD dye where x indicates mol% of CD22 binding peptide density ($0 \leq x \leq 10$). 5 mol% cholesterol was additionally incorporated into a liposomal scaffold to improve stability of liposomal nanoparticles. As a control, non-targeted liposomal nanoparticles were formulated without any targeting peptides (0% peptide density). All the nanoparticles were incorporated with DiD fluorescent dye for quantification using flow cytometry. The size of nanoparticles was characterized by dynamic light scattering (DLS) analysis, showing homogeneous population of nanoparticles with low polydispersity which demonstrates consistency between liposomal nanoparticles (Fig. 4C).

To examine whether the peptides are precisely loaded on CD22 TNP, we investigated loading efficiency by performing RP-HPLC analysis. We prepared CD22 TNPs at 2% peptide density and compared the peptide concentration loaded in the TNPs to the respective theoretical maximum. The results exhibited high loading efficiency (>98%), ensuring that our particles preserve precise number of peptides during nanoparticle preparation (Fig. 4D). Overall, based upon the results from the DLS and loading efficiency analysis, our method allows homogeneous particle population and precise control over the number of targeting peptides, eliminating coupling yield variability to achieve reproducibility in experimental results.

In vitro evaluation of cellular uptake of CD22 TNPs

As shown in the results from the peptide binding assay, PV1 and PV2 showed negligible binding to CD22+ Raji cells while

PV3 showed its binding in the tested concentration range. This result may be due to relatively weaker affinities of PV1 and PV2 peptides to PV3 peptides, resulting in poor monovalent binding efficiency for CD22 receptor. To resolve this problem, multivalent interactions can be utilized to increase the avidity of the peptides which may potentially enhance targeting efficiency. Therefore, we further examined the binding efficiency of the peptides by presenting multivalently on liposomal nanoparticles *via in vitro* cellular uptake assay. Each peptide was loaded at varied peptide density (0.1–4%). Non-targeted liposomal nanoparticles (NP, 0% peptide density) were prepared as controls. DiD fluorescence dye was incorporated for quantification of the cellular uptake by flow cytometry. Raji and Jurkat were used as CD22+ and negative (−) cell line, respectively.[28,40,41] Liposomal nanoparticles with different peptide densities were incubated on Raji and Jurkat for 3 hours, and the cellular uptake was analyzed by flow cytometry.

Our results showed higher cellular uptake of both PV1 and PV2 peptide presenting TNP (TNP^{PV1} and TNP^{PV2}) on Jurkat cells whereas negligible uptake was observed for both nanoparticles in Raji cells, demonstrating that PV1 and PV2 peptides are not selective to CD22 (Fig. 5A and B). In contrast, PV3 peptide presenting TNP (TNP^{PV3}) showed significantly higher uptake on Raji over Jurkat, starting at 2% peptide density. At 2–3%, there was ~3-fold enhancement in the cellular uptake on Raji over Jurkat which further confirmed the selective binding of PV3 peptides on CD22 (Fig. 5C).

To further verify the specificity of PV3 peptides on CD22, we performed the same uptake experiment with an additional CD22− cell line, MOLT-4,[41,42] by varying peptide density from 0.7% to 10%. The results showed no detectable cellular uptake of TNP^{PV3} on MOLT-4 over the peptide densities. In contrast, as the peptide densities increased to 8%, there was up to a drastic 35-fold enhancement in the cellular uptake by Raji over MOLT-4 (Fig. 5D). Combined with the *in vitro* peptide cellular binding assay, the results from the TNP cellular uptake further exhibited the selective binding of PV3 peptides on CD22.

Evaluation of PV3 peptide specificity

To examine the specificity of CD22 PV3 peptides, competitive inhibition experiments with the respective free and soluble PV3 peptides was performed. We prepared TNP^{PV3} at various peptide densities (1–5%). Non-targeted liposomal nano-

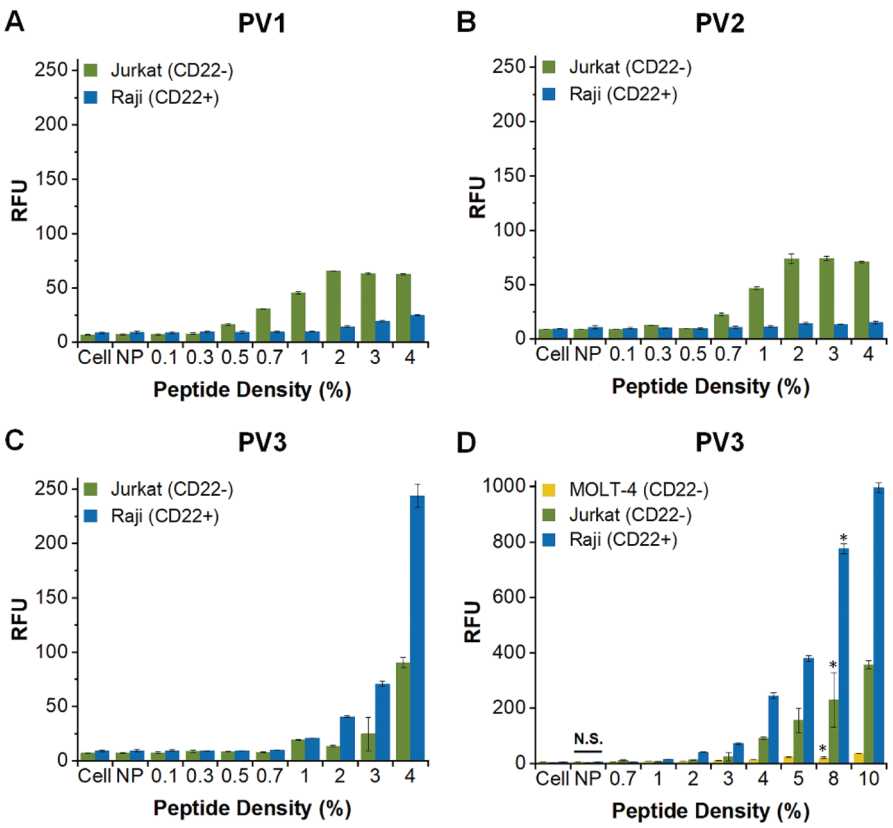

Fig. 5 *In vitro* evaluation of cellular uptake of CD22 TNPs. *In vitro* cellular uptake analysis of TNP formulations of PV1 (A), PV2 (B), or PV3 (C). Raji (CD22+) or Jurkat (CD22−) cells were incubated with near infrared dye (DiD) loaded TNP formulations of varying peptide densities for 3 hours. Internalized DiD fluorescence (RFU) was analyzed *via* flow cytometry. (D) Following initial evaluations, cellular uptake of PV3 presenting TNP (TNP^{PV3}) formulations with increased peptide densities were further investigated. In this experiment, MOLT-4 (CD22−) cell line was used as an additional control. All experiments were done in triplicates and data represents means (±s.d.). No statistical significance was observed among each cell line when treated with NP control (N.S.). On the other hand, there was significant enhancement in cellular uptake of TNP^{PV3} by Raji cells over both Jurkat and MOLT-4 cells (asterisk (*); $p < 0.001$) at 8% peptide density. A Student's *t*-test was used for *P* values.

particles (NP, 0% peptide density) were also prepared as the controls. 0.1 mol% DiD fluorescent dye was incorporated into liposomal nanoparticles to quantify the cellular uptake by flow cytometry. Free PV3 peptides were incubated with Raji at excessive concentration (50 μM), followed by challenging with TNP^{PV3}, and the cellular uptake was analyzed. Our results demonstrated that free PV3 peptides significantly inhibited the cellular uptake of TNP^{PV3} at the peptide density of 4% and 5% by 80% and 60%, respectively (Fig. 6A). This exhibits that PV3 is highly specific to CD22 receptor.

Next, we further evaluated the specificity of PV3 peptides by performing the cellular uptake with scrambled peptides. The randomized sequence of PV3 peptides was prepared and loaded into liposomal nanoparticles ($TNP^{Scr\ PV3}$) at varied peptide density (1–5%), and its cellular uptake on Raji was compared to that of TNP^{PV3}. The results showed significant reduction of the cellular uptake in the $TNP^{Scr\ PV3}$ by approximately 80% at 4% and 5% peptide densities (Fig. 6B). Overall, these results further confirmed the specificity of PV3 peptides to CD22.

Optimization of TNP^{PV3} formulation for enhanced cellular uptake

In several earlier studies, we have shown improved peptide binding activity and cellular uptake with increased peptide hydrophilicity.[43] To enhance the effects of active targeting, we investigated the effects of increasing hydrophilicity of PV3 peptides on the cellular uptake. For this purpose, PV3 peptides were conjugated with various number of lysines (K_N, N = 0–3) adjacent to EG8 or EG18 linker, and we performed cellular uptake assay of liposomal nanoparticles on Raji cell line. The results demonstrated significant uptake enhancement with increased number of oligolysines, presumably due to the increased hydrophilicity of peptides which improved the peptide availability above PEG cloud toward more favorable hydrophilic solvent region (Fig. 7A). In contrast, K_0 and K_1 did not show any cellular uptake, indicating that PV3 peptides need threshold of two oligolysines to significantly enhance the binding efficiency.

The length of EG linkers is another important design parameter. It is critical to use optimized linker length to maximize targeting efficiency.[38,39,44] Therefore, to investigate the effects of linker length, we performed cellular uptake assay of TNP^{PV3} (8% peptide density) on Raji cells with various linker length, including EG0, EG2, EG8, EG18, EG30, and EG45. Non-targeted nanoparticles (0% peptide density) were also prepared as controls. The results demonstrated significant improvement as EG linker were shorter (Fig. 7B). Shorter linkers adopt more linear conformations, thereby enabling more efficient binding to the target receptors by enhancing peptide availability above PEG stealth coating. In contrast, longer linkers, such as EG30 and EG45, tend to have more globular conformation so that peptides are more likely to be buried under PEG cloud, resulting in a reduced peptide availability for target receptor binding. Moreover, compared to shorter linkers, longer linkers are inclined to pay higher conformational entropic penalty, potentially leading to less efficient nanoparticle cellular binding and uptake. On the other hand, EG0 and EG2 linkers showed only minimal cellular uptake, indicating that they are too short to effectively present peptides above PEG cloud. EG8

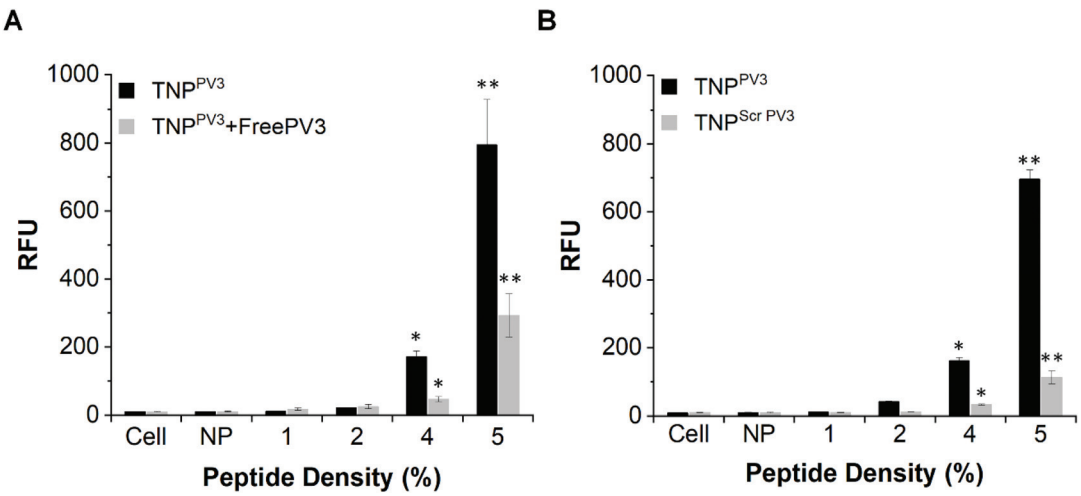

Fig. 6 Evaluation of PV3 peptide specificity. PV3 peptide specificity was evaluated *via* two separate experiments. (A) TNP^{PV3} uptake inhibition *via* excess monovalent PV3 peptide (FreePV3). Raji cells were incubated with unconjugated soluble PV3 30 min prior to administrating fluorescently labeled TNP^{PV3}. After 30 min, TNP^{PV3} was administered to cells with (gray) and without the FreePV3 (black), and let incubate for 3 hours. Cellular uptake, as analyzed *via* flow cytometry, was effectively inhibited with the monovalent peptide. Asterisks show statistical comparisons of cellular uptake in groups between TNP^{PV3} and TNP^{PV3} with FreePV3 at 4% (*) and 5% (**) peptide density, respectively ($P < 0.001$). (B) Comparison of TNP^{PV3} with TNP presenting scramble PV3 peptide ($TNP^{Scr\ PV3}$). Raji cells were incubated with either TNP^{PV3} or $TNP^{Scr\ PV3}$ for 3 hours. Cellular uptake analysis *via* flow cytometry showed the scrambled peptide was ineffective in targeting. All experiments were conducted in triplicates and data shows means (±s.d.). Statistical difference of nanoparticle cellular uptake was shown in groups between TNP^{PV3} and $TNP^{Scr\ PV3}$ at 4% (*) and 5% (**) peptide density, respectively ($P < 0.001$). All statistical analyses were performed using a Student's *t*-test.

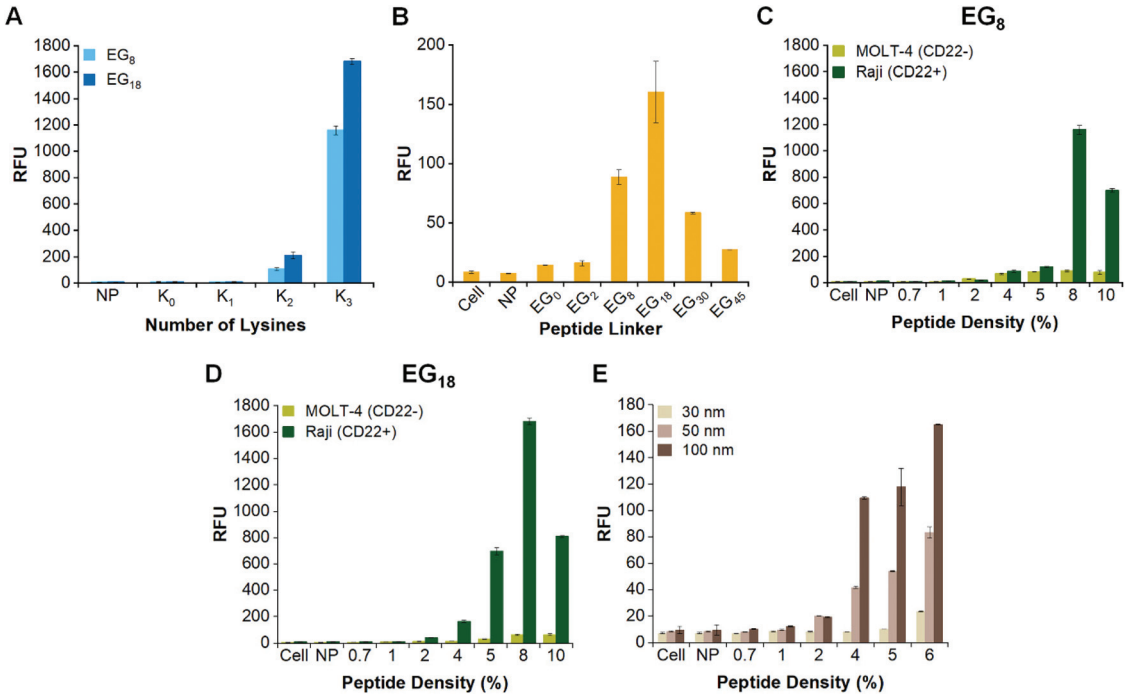

Fig. 7 Optimization of TNP^{PV3} formulation for enhanced cellular uptake. Several nanoparticle design parameters were evaluated for their individual effects on cellular targeting and uptake to find optimal TNP^{PV3} formulation, including (A) oligolysines, (B) peptide EG linker length, (C and D) peptide density, and (E) nanoparticle size. All experiments were performed in triplicates using fluorescently labeled TNPs and *in vitro* cellular uptake assay with Raji cells. Data represents means (±s.d.).

was found to be the minimum linker length to efficiently present PV3 peptides, allowing them in a proper conformation to bind CD22. Overall, EG18 was determined to be the optimized linker length for the effective peptide presentation to maximize *in vitro* cellular uptake of TNP^{PV3}.

Next, we further examined the valency effects with EG8 and EG18 linkers to evaluate optimized peptide density to further maximize the cellular uptake of TNP^{PV3}. For this purpose, we performed cellular uptake assay with TNP^{PV3} of various peptide densities from 0.7% to 10% with EG8 and EG18 linkers on Raji and MOLT-4 cell lines. The results showed higher cellular uptake over the increased peptide density. This is due to the enhanced avidity which provided nanoparticles with longer binding residence time on CD22, resulting in improved binding efficiency and cellular uptake. Furthermore, the results demonstrated that TNP^{PV3} of EG18 linker needed less peptide density (5%) than EG8 linker (8%) for significant cellular uptake enhancement, presumably due to its better presentation of peptides over PEG cloud to enhance binding efficiency (Fig. 7C and D). This may be attributed to a short sequence of PV3 peptides, requiring longer linkers of EG18 over EG8 to reach binding sites of CD22. Besides varying peptide densities, particle size is another significant factor to modify valency on nanoparticles. As seen in Fig. 7E, larger nanoparticle size demonstrated enhanced cellular uptake by presenting a greater number of peptides even at the same peptide density. More importantly, larger nanoparticles with lower peptide density showed similar-to-higher cellular uptake to that of smaller nanoparticles with higher peptide density. This suggests a significant advantage in the *in vivo* application of TNP^{PV3}. Larger nanoparticles (up to ~200 nm) with reduced peptide density have shown improved *in vivo* circulation half-lives while minimizing RES effects, suggesting TNP^{PV3} as a potential drug delivery vehicle to effectively target B-cell malignancies while continuously circulating in the blood stream.

Conclusions

In this report, our goal was to overcome one of the most significant hurdles in targeted treatments for B-cell malignancies, the on-target/off-tumor toxic effect, and to achieve cancer cell selectivity. Since the toxic side effects are primarily attributed to high-affinity and highly specific targeting moieties that non-selectively bind to their target receptors regardless of whether positioned on malignant B-cells or healthy B-cells, our strategy was utilizing a CD22-specific peptide (PV3) with a moderate affinity. We identified several CD22 binding peptides by analyzing the hypervariable loops from the 3D crystal structure of anti-CD22 antibody (epratuzumab)-CD22 receptor complex. The sequences were identified through studying the amino acid residues at the interacting surfaces of the antigen–antibody complex, and rationally predicting and ranking the relative affinities of these sequences. Given the crystal structure of antigen–antibody complex was available, this approach was very efficient for the target peptide identification since it was a

significantly time and cost-effective method, as compared to other techniques such as phage display, microarray, *etc*.

Traditionally, TNP drug delivery systems are developed to treat solid tumors, particularly due to enhanced permeability and retention (EPR) effect.[45] In such applications, one of the most weighty challenges is the effective delivery of drug-loaded TNPs into the depths of tumor tissue to hit the residing tumor cells. In this regard, many TNPs are designed to be as small a size as possible since smaller particles reportedly have an advantage in tumor penetration. In parallel, these TNPs are designed to overcome binding site barrier (BSB) phenomenon by presenting fewer targeting elements.[46] Since high avidity due to high valency results in most TNPs targeting only the tumor cells immediately adjacent to angiogenic vasculature, it leads to reduced efficacy. In comparison, designing TNPs to target blood cancer cells can be more complicated, hence different strategies need to be implemented because these cells remain in systemic circulation and do not form solid legions.

In this study, we introduced a strategy for effective targeting of malignant CD22+ B-cells through investigating the impact of individual TNP design parameters on *in vitro* cellular uptake. As demonstrated in results of uptake experiments using Raji cells (CD22+), avidity can be enhanced by increasing targeting peptide valency, to achieve efficient and rapid targeting. Contrary to targeting solid tumors, where it causes a significant hurdle, BSB phenomenon should be of no concern when increasing the avidity of TNPs for blood cancers. Nevertheless, at elevated valency, this strategy begins to show evidence for sacrificed selectivity for target blood cancer cells as increased TNP uptake by Jurkat cells (CD22−) was observed at higher peptide densities (Fig. 5). Since this unintentional cellular uptake can lead to toxic side-effects for blood cancer patients, it was critical to identify the ideal peptide density that improves selectivity for target blood cancer cells by comparing uptake by CD22+ and CD22− cells.

Increasing particle size is another strategy we used to increase valency and improve avidity. We demonstrated that compared to smaller particles, TNPs of larger size had enhanced uptake by CD22+ cells at any given density due to higher valency (*e.g.*, 600 *vs.* 2400 at the same 6% peptide density in 50 nm and 100 nm, respectively). Moreover, larger particles typically have a prolonged *in vivo* circulation half-life, improving the probability of TNPs encountering target blood cancer cells. Nevertheless, when converting to *in vivo* models, particle size requires careful assessment since increasing particle size may result in not only off-target binding to healthy cells but also RES clearance by opsonization. In current study, we observed that cellular uptake of larger TNPs with lower peptide density was at a similar-to-higher level to that of smaller TNPs with higher peptide density. Hence, TNPs of larger size with low peptide density can be designed to have an extended *in vivo* circulation half-life as well as optimized avidity to achieve enhanced CD22+ malignant B-cell uptake, while preventing unintentional off-target binding and RES clearance.

Furthermore, targeting efficiency of TNPs for blood cancer cells can be improved by controlling additional design parameters such as peptide linker length (EG_N) and the number of lysines. Under circumstances where blood cancer cells remain in systemic circulation, it is critical for TNPs to bind with rapid kinetics to the target receptors upon encountering the blood cancer cells. In this study, we demonstrated that shorter EG linkers increased CD22+ blood cancer cell uptake due to their conformation adopting more rigid and linear structure relative to longer linkers. In addition, we also verified that increased number of lysine residues adjacent to PV3 peptide improved CD22+ cellular uptake owing to favorable partitioning into aqueous phase. Taking all into account, we expect that shorter linkers with oligolysines enable TNPs to present targeting peptides more effectively above PEG cloud to be ready for immediately interacting with target blood cancer cells.

In summary, we confidently report the effects of several nanoparticle design parameters on CD22+ malignant B-cell uptake *in vitro* to identify an optimal TNP formulation that potentially enables efficient targeting for CD22+ blood cancer cells *in vivo*. Although we identified three lysines, EG18 linker, and 8% peptide density with 100 nm to be the optimal TNP^{PV3} design parameters *in vitro*, this exact design may not provide the optimal *in vivo* outcomes given the complexity of *in vivo* environment including a shear blood flow, off-target binding to healthy cells, opsonization, RES clearance, *etc*. In future experiments, building upon *in vitro* results as a starting point, we will examine how the parameters affect *in vivo* using an animal model to *in vivo* optimize our TNP^{PV3} drug delivery systems. Following *in vivo* optimization, we will incorporate anti-neoplastic drug molecules to the optimized TNP^{PV3} platform and at the end evaluate their *in vivo* anti-cancer efficacy and toxicity. We predict that optimized drug loaded TNP^{PV3} both *in vitro* and *in vivo* will increase anti-cancer efficacy *via* enhanced selective uptake by CD22+ blood cancer cells relative to non-targeted drug loaded NPs and conventional treatments.

Conflicts of interest

There are no conflicts of interest to declare.

Acknowledgements

We thank the Mass Spectrometry and Proteomics Facility in the University of Notre Dame for MS Instrumentation and the Center for Environmental Science and Technology for DLS instrument. This work was supported by the Walther Cancer Research Foundation for the PreClinical Testing Facility Proof of Concept Grant.

References

1 N. K. Mittal, H. Bhattacharjee, B. Mandal, P. Balabathula, L. A. Thoma and G. C. Wood, *J. Drug Targeting*, 2014, **22**, 372–386.

2 G. Salles, M. Barrett, R. Foà, J. Maurer, S. O'Brien, N. Valente, M. Wenger and D. G. Maloney, *Adv. Ther.*, 2017, **34**, 2232–2273.
3 S. Ayyappan and K. Maddocks, *J. Hematol. Oncol.*, 2019, **12**, 82.
4 J. F. Rossi, *BioMed Res. Int.*, 2015, **2015**, 217593.
5 S. Crisci, R. Di Francia, S. Mele, P. Vitale, G. Ronga, R. De Filippi, M. Berretta, P. Rossi and A. Pinto, *Front. Oncol.*, 2019, **9**, 443.
6 J. N. Brudno and J. N. Kochenderfer, *Nat. Rev. Clin Oncol.*, 2018, **15**, 31–46.
7 S. J. Schuster, J. Svoboda, E. A. Chong, S. D. Nasta, A. R. Mato, Ö. Anak, J. L. Brogdon, I. Pruteanu-Malinici, V. Bhoj, D. Landsburg, M. Wasik, B. L. Levine, S. F. Lacey, J. J. Melenhorst, D. L. Porter and C. H. June, *N. Engl. J. Med.*, 2017, **377**, 2545–2554.
8 J. N. Brudno and J. N. Kochenderfer, *Blood*, 2016, **127**, 3321–3330.
9 S. A. Grupp, M. Kalos, D. Barrett, R. Aplenc, D. L. Porter, S. R. Rheingold, D. T. Teachey, A. Chew, B. Hauck, J. F. Wright, M. C. Milone, B. L. Levine and C. H. June, *N. Engl. J. Med.*, 2013, **368**, 1509–1518.
10 J. N. Kochenderfer, M. E. Dudley, S. A. Feldman, W. H. Wilson, D. E. Spaner, I. Maric, M. Stetler-Stevenson, G. Q. Phan, M. S. Hughes, R. M. Sherry, J. C. Yang, U. S. Kammula, L. Devillier, R. Carpenter, D. A. Nathan, R. A. Morgan, C. Laurencot and S. A. Rosenberg, *Blood*, 2012, **119**, 2709–2720.
11 S. S. Neelapu, S. Tummala, P. Kebriaei, W. Wierda, C. Gutierrez, F. L. Locke, K. V. Komanduri, Y. Lin, N. Jain, N. Daver, J. Westin, A. M. Gulbis, M. E. Loghin, J. F. de Groot, S. Adkins, S. E. Davis, K. Rezvani, P. Hwu and E. J. Shpall, *Nat. Rev. Clin Oncol.*, 2018, **15**, 47–62.
12 T. Gargett and M. P. Brown, *Front. Pharmacol.*, 2014, **5**, 235.
13 N. Mezzaroba, S. Zorzet, E. Secco, S. Biffi, C. Tripodo, M. Calvaruso, R. Mendoza-Maldonado, S. Capolla, M. Granzotto, R. Spretz, G. Larsen, S. Noriega, M. Lucafò, E. Mansilla, C. Garrovo, G. H. Marín, G. Baj, V. Gattei, G. Pozzato, L. Núñez and P. Macor, *PLoS One*, 2013, **8**, e74216.
14 K. Loomis, B. Smith, Y. Feng, H. Garg, A. Yavlovich, R. Campbell-Massa, D. S. Dimitrov, R. Blumenthal, X. Xiao and A. Puri, *Exp. Mol. Pathol.*, 2010, **88**, 238–249.
15 W. C. Chen, G. C. Completo, D. S. Sigal, P. R. Crocker, A. Saven and J. C. Paulson, *Blood*, 2010, **115**, 4778–4786.
16 N. Satake, C. Duong, C. Chen, G. A. Barisone, E. Diaz, J. Tuscano, D. M. Rocke, J. Nolta and N. Nitin, *Br. J. Haematol.*, 2014, **167**, 487–499.
17 M. C. Palanca-Wessels, A. J. Convertine, R. Cutler-Strom, G. C. Booth, F. Lee, G. Y. Berguig, P. S. Stayton and O. W. Press, *Mol. Ther.*, 2011, **19**, 1529–1537.
18 F. M. Uckun, S. Qazi, H. Ma, L. Yin and J. Cheng, *EBioMedicine*, 2014, **1**, 141–155.
19 W. W. Cheng and T. M. Allen, *J. Controlled Release*, 2008, **126**, 50–58.
20 S. Jiang, X. Wang, Z. Zhang, L. Sun, Y. Pu, H. Yao, J. Li, Y. Liu, Y. Zhang and W. Zhang, *Int. J. Nanomed.*, 2016, **11**, 5505–5518.
21 V. Krishnan, X. Xu, D. Kelly, A. Snook, S. A. Waldman, R. W. Mason, X. Jia and A. K. Rajasekaran, *Mol. Pharm.*, 2015, **12**, 2101–2111.
22 W. K. Nevala, J. T. Butterfield, S. L. Sutor, D. J. Knauer and S. N. Markovic, *Sci. Rep.*, 2017, **7**, 45682.
23 C. Chittasupho, *Ther. Delivery*, 2012, **3**, 1171–1187.
24 D. Rosenblum, N. Joshi, W. Tao, J. M. Karp and D. Peer, *Nat. Commun.*, 2018, **9**, 1410.
25 E. Ruoslahti, *Adv. Mater.*, 2012, **24**, 3747–3756.
26 G. Vauquelin and S. J. Charlton, *Br. J. Pharmacol.*, 2013, **168**, 1771–1785.
27 J. A. Walker and K. G. Smith, *Immunology*, 2008, **123**, 314–325.
28 W. Haso, D. W. Lee, N. N. Shah, M. Stetler-Stevenson, C. M. Yuan, I. H. Pastan, D. S. Dimitrov, R. A. Morgan, D. J. FitzGerald, D. M. Barrett, A. S. Wayne, C. L. Mackall and R. J. Orentas, *Blood*, 2013, **121**, 1165–1174.
29 L. Sullivan-Chang, R. T. O'Donnell and J. M. Tuscano, *BioDrugs*, 2013, **27**, 293–304.
30 N. N. Shah, M. S. Stevenson, C. M. Yuan, K. Richards, C. Delbrook, R. J. Kreitman, I. Pastan and A. S. Wayne, *Pediatr. Blood Cancer*, 2015, **62**, 964–969.
31 J. Rosenthal, A. S. Naqvi, M. Luo, G. Wertheim, M. Paessler, A. Thomas-Tikhonenko, S. R. Rheingold and V. Pillai, *Am. J. Hematol.*, 2018, **93**, E352–E355.
32 J. Ereño-Orbea, T. Sicard, H. Cui, M. T. Mazhab-Jafari, S. Benlekbir, A. Guarné, J. L. Rubinstein and J. P. Julien, *Nat. Commun.*, 2017, **8**, 764.
33 J. F. Stefanick, D. T. Omstead, T. Kiziltepe and B. Bilgicer, *Nanoscale*, 2019, **11**, 4414–4427.
34 N. J. Alves, W. Cusick, J. F. Stefanick, J. D. Ashley, M. W. Handlogten and B. Bilgicer, *Analyst*, 2013, **138**, 4746–4751.
35 D. C. Ekiert, G. Bhabha, M. A. Elsliger, R. H. Friesen, M. Jongeneelen, M. Throsby, J. Goudsmit and I. A. Wilson, *Science*, 2009, **324**, 246–251.
36 D. C. Ekiert, R. H. Friesen, G. Bhabha, T. Kwaks, M. Jongeneelen, W. Yu, C. Ophorst, F. Cox, H. J. Korse, B. Brandenburg, R. Vogels, J. P. Brakenhoff, R. Kompier, M. H. Koldijk, L. A. Cornelissen, L. L. Poon, M. Peiris, W. Koudstaal, I. A. Wilson and J. Goudsmit, *Science*, 2011, **333**, 843–850.
37 H. Xiao, T. Guo, M. Yang, J. Qi, C. Huang, Y. Hong, J. Gu, X. Pang, W. J. Liu, R. Peng, J. McCauley, Y. Bi, S. Li, J. Feng, H. Zhang, X. Zhang, X. Lu, J. Yan, L. Chen, Y. Shi, W. Chen and G. F. Gao, *Cell Discovery*, 2019, **5**, 21.
38 J. F. Stefanick, J. D. Ashley and B. Bilgicer, *ACS Nano*, 2013, **7**, 8115–8127.
39 J. F. Stefanick, J. D. Ashley, T. Kiziltepe and B. Bilgicer, *ACS Nano*, 2013, **7**, 2935–2947.
40 J. M. Tuscano, J. Kato, D. Pearson, C. Xiong, L. Newell, Y. Ma, D. R. Gandara and R. T. O'Donnell, *Cancer Res.*, 2012, **72**, 5556–5565.
41 M. Sartor and K. Bradstock, *Cytometry*, 1994, **18**, 119–122.

42 S. Takagi, K. Fujikawa, T. Imai, N. Fukuhara, K. Fukudome, M. Minegishi, S. Tsuchiya, T. Konno, Y. Hinuma and O. Yoshie, *Int. J. Cancer*, 1995, **61**, 706–715.
43 J. F. Stefanick, T. Kiziltepe and B. Bilgicer, *J. Biomed. Nanotechnol.*, 2015, **11**, 1418–1430.
44 O. Tirosh, Y. Barenholz, J. Katzhendler and A. Priev, *Biophys. J.*, 1998, **74**, 1371–1379.
45 A. D. Wong, M. Ye, M. B. Ulmschneider and P. C. Searson, *PLoS One*, 2015, **10**, e0123461.
46 T. M. Allen, *Nat. Rev. Cancer*, 2002, **2**, 750–763.